Epitaxial Dimers and Auger-Assisted Detrapping in PbS Quantum Dot Solids

Epitaxial Dimers and Auger-Assisted De-Trapping in PbS Quantum Dot Solids

Rachel H. Gilmore[1], Yun Liu[2], Wenbi Shcherbakov-Wu[4], Nabeel S. Dahod[1], Elizabeth M.Y. Lee[1], Mark C. Weidman[1], Huashan Li[2], Joel Jean[3], Vladimir Bulović[3], Adam P. Willard[4], Jeffrey C. Grossman[2], William A. Tisdale[1]*

[1]Department of Chemical Engineering, Massachusetts Institute of Technology, Cambridge, Massachusetts, 02139, USA.

[2]Department of Materials Science and Engineering, Massachusetts Institute of Technology, Cambridge, Massachusetts 02139, USA.

[3]Department of Electrical Engineering and Computer Science, Massachusetts Institute of Technology, Cambridge, Massachusetts, 02139, USA.

[4]Department of Chemistry, Massachusetts Institute of Technology, Cambridge, Massachusetts 02139, USA.

*Correspondence to: tisdale@mit.edu

Abstract: Electronic trap states limit the overall power conversion efficiency of quantum dot (QD) solar cells by inhibiting charge carrier transport and reducing the open-circuit voltage. Here, we explore the dynamic interaction of charge carriers between band edge states and sub-band trap states using broadband transient absorption spectroscopy. In monodisperse arrays of 4-5 nm diameter PbS QDs, we observe an optically active trap state ~100-200 meV below the band edge that occurs at a frequency of 1 in ~2500 QDs. Uncoupled QD solids with oleic acid ligands show trap-to-ground-state recombination that resembles Auger recombination. In electronically coupled QD solids, we observe entropically-driven uphill thermalization of trapped charge carriers from the trap state to the band edge *via* two distinct mechanisms: Auger-assisted charge transfer (~35 ps) and thermally activated hopping (~500 ps). Photophysical characterization combined with atomistic simulations and high-resolution transmission electron microscopy suggest that these

states arise from epitaxially fused pairs of QDs – rather than electron or hole traps at the QD surface – offering new strategies for improving the efficiency of QD solar cells.

Keywords: *Nanocrystal, lead sulfide, transport, trap state, transient absorption*

Introduction

Colloidal nanocrystal quantum dots (QDs) are promising building blocks for next-generation optoelectronic technologies because of their tunable size and shape, size-dependent optical properties, and flexible ligand chemistry. However, challenges associated with the synthesis and formation of electronically coupled QD solids remain.[1, 2] In particular, mid-bandgap trap states have garnered substantial attention because they limit photovoltaic device efficiencies by reducing the open-circuit voltage[3] and acting as charge carrier recombination sites.[4] Trap states are involved in charge carrier transport, either directly through mid-gap transport[5, 6] or through multiple trapping and release steps.[7, 8] The electronic characteristics of trap states are observed to vary with ligand treatments,[9, 10] air exposure,[11] and other oxidation treatments,[12] prompting speculation that trap states are associated with structural defects or unpassivated sites on the QD surface, or with strongly coupled QD aggregates.[4, 13-15]

Here, we use broadband near-infrared transient absorption (TA) spectroscopy to study the dynamics of charge carrier de-trapping in PbS QD solids. By employing highly monodisperse QDs (size dispersity 1-3%), we are able to spectrally distinguish the trap state from the normal inhomogeneous distribution of band-edge states. In electronically coupled QD solids, we observe efficient uphill thermalization of trapped charge carriers to the band edge transport level. De-trapping is entropically favored due to the large excess density of band edge states relative to trap states. We observe two kinetic mechanisms of de-trapping: (1) a fluence-dependent, temperature-independent Auger-assisted electron transfer process that occurs on a timescale of ~35 ps, and (2) a fluence-independent, temperature-dependent thermally-assisted hopping process that occurs on a time scale of ~500 ps at room temperature. From temperature-dependent photoluminescence (PL) measurements, we infer a trap state density of 1 in ~2500 QDs, which is consistent with

literature reports for thiol-treated QD solids.[10, 11, 16] In addition, we use Kinetic Monte Carlo (KMC) simulations to confirm the entropically-driven charge carrier de-trapping mechanism.

Upon direct photoexcitation of the trap state in QD solids with insulating oleic acid ligand we observe clear signatures of Auger recombination, revealing a trap state degeneracy, bi-exciton decay time, and absorption cross section similar to the band edge state of a single QD – rather than an electron or hole surface trap. TEM image analysis confirms the absence of unusually large QDs but also reveals the infrequent occurrence of epitaxially-fused QD dimers, which can explain our findings. Strong electronic coupling between two fused QDs can generate new states lower in energy by ~100-200 meV relative to the single QD band gap[15, 17] (1.08 eV for 4.9 nm diameter QDs and 1.3 eV for 4.2 nm diameter QDs, as studied here). Furthermore, density functional theory (DFT) calculations of PbS QD dimers epitaxially attached on the (100) facet exhibit optical properties and energy shifts that are consistent with spectroscopic results.

Direct Photoexcitation of the Trap State

PbS QDs were synthesized according to previously published procedures,[18, 19] dispersed in toluene, and spin coated onto glass substrates for TA measurements or single crystal quartz substrates for temperature-dependent PL measurements. To make electronically coupled solids, QD films were ligand exchanged with ethanethiol in a nitrogen glovebox (see Methods).[20]

To probe charge carrier de-trapping kinetics, we performed experiments in which we directly photoexcited the ground-to-trap state transition using a sub-bandgap laser pulse, and subsequently tracked the dynamic occupation of the trap and band edge states using ultrafast transient absorption (TA) spectroscopy (Figure 1a and Methods). In Figure 1b, the trap state at 1.06 eV of 4.2 nm diameter (1.3 eV) QDs is excited with a 0.99 eV pump laser pulse. Immediately

following photoexcitation, only the trap state is occupied. The band edge bleach feature subsequently grows in over the next ~500 ps as the intensity of the trap state bleach feature decreases, signaling population transfer from trap to band edge. Spectral slices (Figure 1c) clearly show only the trap state bleach at early times, and the population of both states at later times. The energy of the band edge bleach signal at 1.24 eV is the same as the thermalized energy of the band edge TA signal when excited well above the band gap.[21] The integrated intensities of the band edge and trap state bleach features as a function of time are shown in Figure 1d. By ~2.0 ns, equilibrium between the trap state and the band edge has been reached and the ratio of the intensity of the two bleach features subsequently remains constant. If we assume that the decrease in bleach intensity of the trap state is entirely due to carriers de-trapping to the band edge state, we estimate that the trap state absorption cross section is approximately two to three times greater than the band edge absorption cross section.

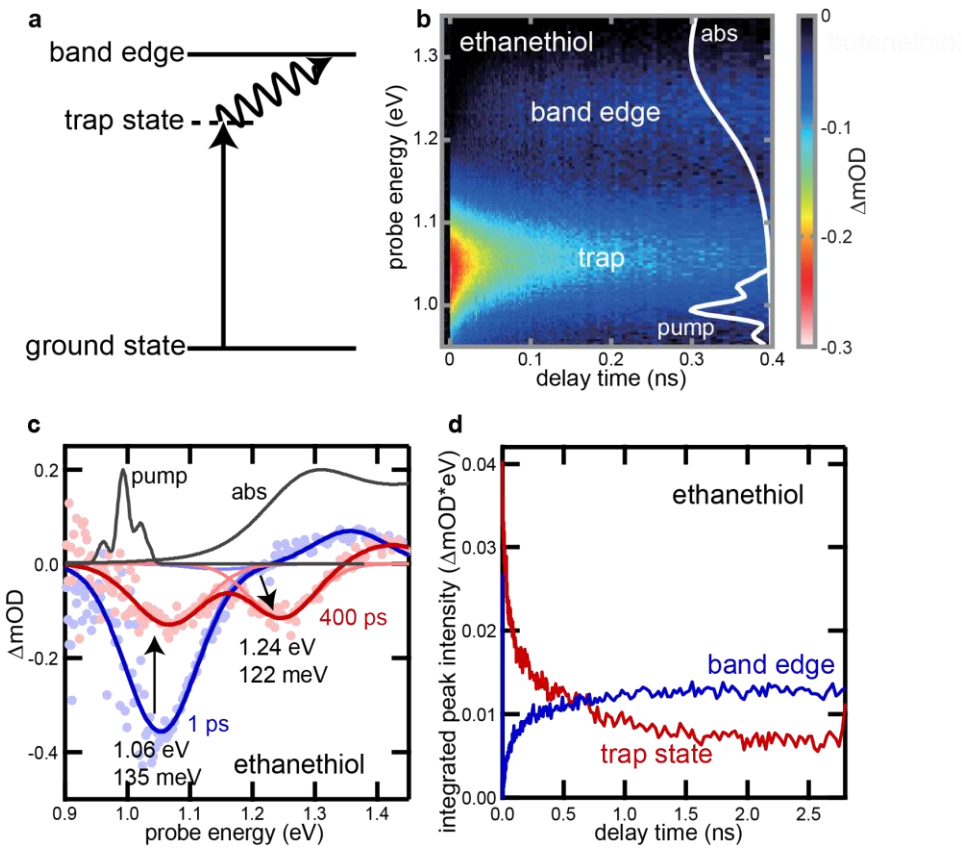

Figure 1. *Uphill thermalization of trapped charge carriers.* (a) Energy level diagram showing direct excitation of the trap state followed by uphill thermalization to the band edge. (b) TA color plots showing spectral dynamics following excitation of the trap state in QD solids (d = 4.2 nm, δ=2.1-3.0%) as a function of ligand length. The pump spectra and QD solution absorption spectra are overlaid as solid white lines for reference. (c) Selected TA spectra at 1 ps and 400 ps following photoexcitation of the trap state shown in panel b. (d) Integrated peak intensities as a function of delay time for the ethanethiol treated solid shown in (b).

The behavior shown in Figure 1 is characteristic of an entropically-driven de-trapping process. If the density of states at the band edge is much larger than the density of trap states ($\frac{DOS_{BE}}{DOS_{trap}} > e^{-(E_{BE}-E_{trap})/k_bT}$), then charge carriers are more likely to be found at the band edge than the trap level once equilibrium is reached. In this case, entropy maximization drives charge carriers uphill in energy.

It is noteworthy that, when the trap state is selectively excited, no bleach signal is observed initially at the band edge energy. The conduction and valence band edges have the same

degeneracy in lead chalcogenide QDs, so the electrons and holes contribute approximately equally to the TA band edge bleach signal[22]. The absence of a bleach feature at the band edge energy implies that the excitation does not involve an electron or hole in a core band edge level of a typical QD (for instance, a transition from a band edge level to an empty surface state), which would immediately contribute a partial bleach at the band edge energy.

Spectral signatures of the trap state are also observed in QD solids with oleic acid ligands, but uphill thermalization to the band edge does not occur (Figure 2e). Exciting the trap state in QD solids with varying length thiol ligands (Figure 2a-d), we see that de-trapping occurs only for the shortest two ligands, ethanethiol and butanethiol, but not for the longer octanethiol or dodecanethiol ligands. From these results, we conclude that electronic coupling and fast diffusion away from the trap site is needed to depopulate the trap state (see also Figure S1). Additionally, we note that the trap state bleach intensity in the thiol-treated samples is consistently ~3 times greater than that in the oleic acid sample, indicating an increase in the trap state density following ligand exchange.

To gain a better understanding of the energy distribution of the trap state as compared to the band edge state, we vary the excitation wavelength in the ethanethiol QD solid. As the excitation energy is increased from 0.99 eV (Figure 2f) to 1.03 eV (Figure 2g) and 1.08 eV (Figure 2h), the excitation pulse begins to overlap with the low energy tail of the QD size distribution (Figure S2). The expected blue-shift of charge carriers in the band-edge manifold toward the thermalized equilibrium average energy (white dashed line) is then observed in addition to depopulation of the trap state.

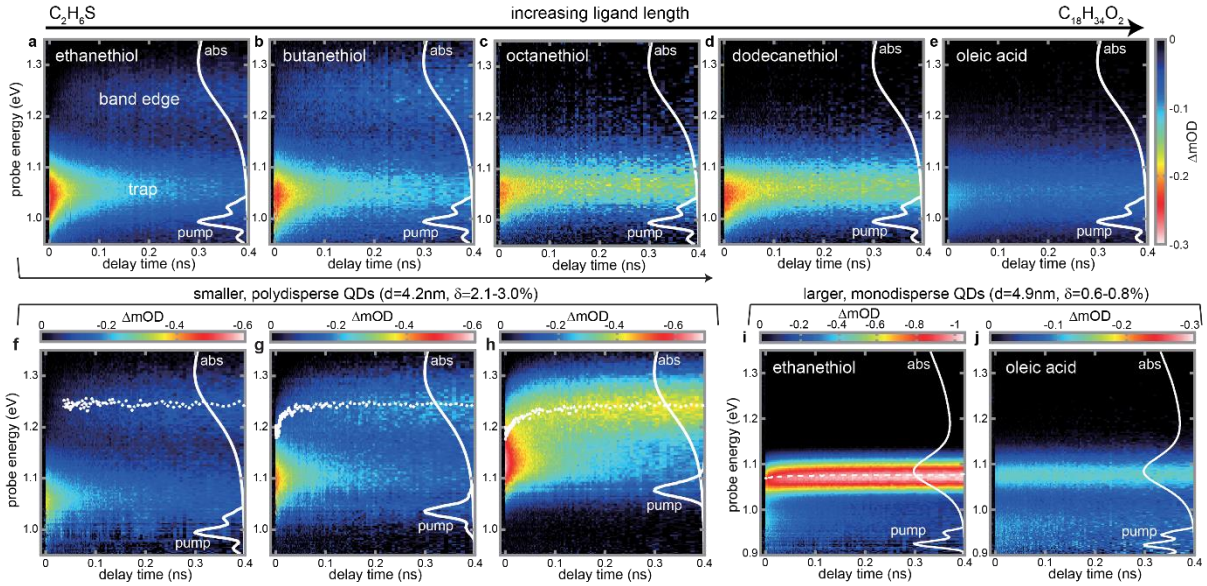

Figure 2. *Spectral dynamics following direct photoexcitation of the trap state at 300 K.* (a-e) TA color plots showing spectral dynamics following excitation of the trap state in QD solids (d = 4.2 nm, δ=2.1-3.0%) as a function of ligand length. The pump spectra and QD solution absorption spectra are overlaid as solid white lines for reference. Panel (a) is a replica of panel (b) from Figure 1. (f-h) TA color plots showing spectral dynamics as the excitation wavelength is tuned closer to the band edge. (i-j) TA color plots showing spectral dynamics in larger, more monodisperse QD solids (d = 4.9 nm, δ=0.6-0.8%) whose band edge absorption peak is near the homogeneous limit. The laser excitation pulse is sufficiently broad to excite both the trap state and the band edge state.

Similar behavior is also observed in more monodisperse ensembles of larger sized QDs (4.9 nm, 1.08 eV), but the trap state and band edge state are too close in energy to be selectively excited with our femtosecond laser excitation pulses (Figure 2i-j, Figure S2). However, two spectrally distinct features are observed in the TA spectrum for both the oleic acid capped QDs and the thiol-exchanged QDs. The monodispersity of this QD batch (spectrally narrow band edge bleach feature allowing clear separation from the trap state feature) and the excitation energy dependence shown in Figure 2f-h clearly demonstrate that the trap state is a distinct state and not simply the tail of the size distribution.[23, 24] We also performed photothermal deflection spectroscopy, which showed continuous absorption in the sub-bandgap region, consistent with the existence of separate manifold of trap states (Figure S3).[25] Furthermore, the trap state absorption

bleach at 0.97 eV in these larger QDs is lower in energy than in the smaller QDs, and closer in energy to the band edge peak (shallower depth), indicating a size-dependence of the trap state energy (Figure S2). We also note that these trap states are observed with other common ligands, such as 3-mercaptopropionic acid or tetrabutylammonium iodide (Figure S4), further indicating that they are a property of the QD solid, and not specific to any surface treatment.

Kinetics of De-Trapping

To learn more about the nature of the trap state and the de-trapping process, we turn to analysis of the de-trapping and recombination kinetics. Figure 3a presents the integrated trap state bleach intensity in an oleic acid QD solid as a function of delay time following trap state excitation for several different laser fluences. In this sample, only trap-to-ground-state recombination is observed because QD-QD electronic coupling is too weak for uphill thermalization, which requires carrier transport away from the trapping site. The initial bleach intensity increases with fluence, as does the fraction of the intensity that decays within the first ~100 ps. These dynamics are reminiscent of Auger recombination dynamics[26] in isolated QDs in solution (Figure S5a). Indeed, the time constants of the multi-exciton decay are in line with the band edge multi-exciton decay in PbS QDs (Figure 3b), which becomes faster for smaller QDs.[26] The absorption cross section of the trap state can be estimated from the intensity-dependent measurements, and yields a value of 8×10^{-16} cm^2 (Figure 3c), which is the same order of magnitude as the band edge state (Figure S5b,c).[27, 28] Thus, based on their photophysical properties, the trap states behave much more like large QDs than like charge-separated surface defects.

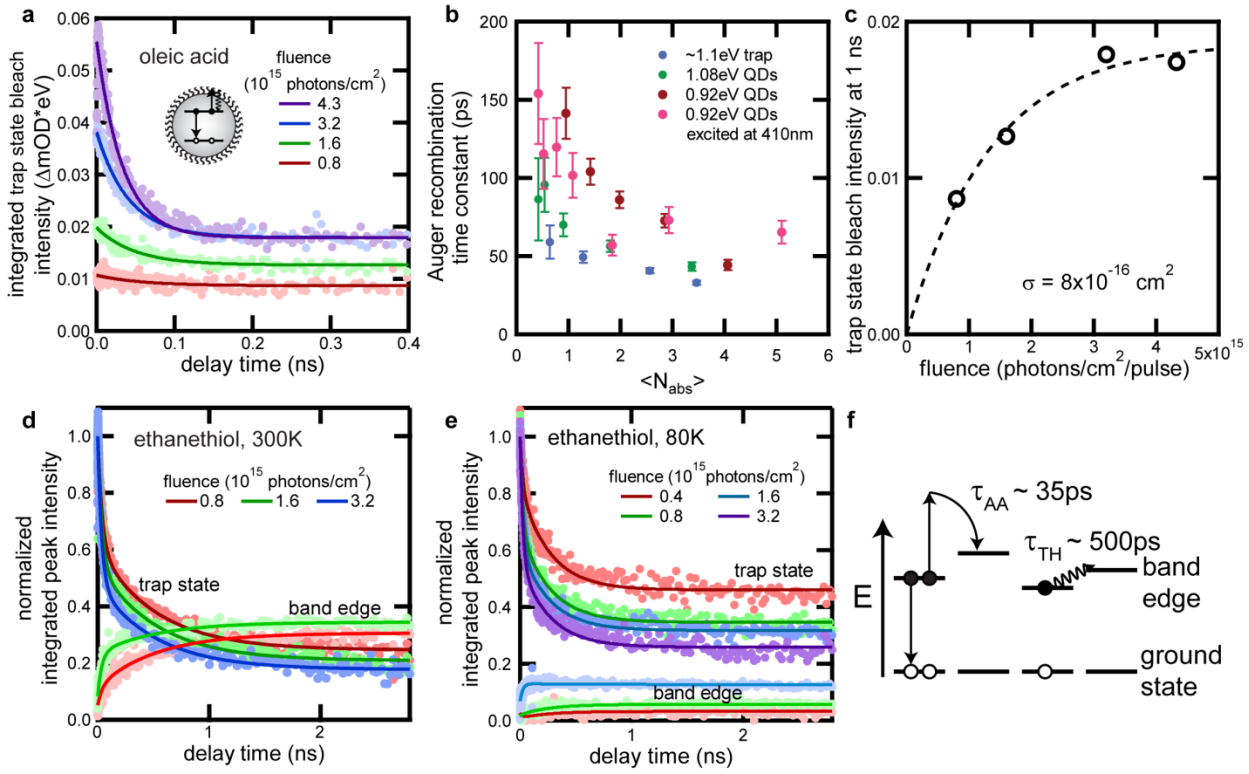

Figure 3. *Analysis of de-trapping kinetics.* (a) Trap state bleach intensity in QD solid with oleic acid ligands as a function of delay time and excitation power showing dynamics characteristic of Auger recombination. (b) Trap state decay time constant in oleic acid capped QDs as a function of number of excitons absorbed per QD, and comparison to Auger recombination in QDs with similar band gap energy. (c) Bleach intensity at 1 ns as a function of excitation fluence. Experimental data are shown as open circles and a model fit to determine the absorption cross section is shown by the dashed line. (d, e) Comparison of trap state and band edge bleach dynamics in ethanethiol-treated QD solid as a function of trap state excitation fluence at 300 K and at 80 K. (f) Schematic showing two observed de-trapping mechanisms. AA = Auger-assisted; TH = thermally activated.

De-trapping kinetics in electronically-coupled QD solids (Figure 3d,e) resemble dynamics one might expect for larger QDs in a matrix of smaller QDs. Figure 3d presents the normalized integrated trap and band edge bleach intensities as a function of delay time following direct trap state excitation for different excitation fluences at 300 K. The decay of the trap signal and growth of the band edge signal mirror each other, as expected for population transfer from the trap state manifold to the band edge. As the excitation fluence increases, the magnitude of population transfer from the trap to the band edge state increases.

The de-trapping process follows two timescales, with a fast component that increases in magnitude with increasing fluence and a slow component that does not depend on fluence. Fluence-dependent measurements at 80 K (Figure 3e) freeze out the slow de-trapping mechanism, but reveal that the fast de-trapping mechanism is temperature-independent. The fast (~35 ps) de-trapping process occurs on similar time scales as the Auger recombination process observed in oleic acid QD solids, suggesting that the temperature-independent, fluence-dependent fast de-trapping process is an Auger-assisted electron transfer event.[29, 30] As illustrated in Figure 3f, when two excitons occupy the same trap site, Auger recombination can generate a single energetic (hot) charge carrier, which is able to rapidly transfer to a neighboring QD before cooling back to the band edge. We assign the slower (~500 ps) de-trapping mechanism to thermally-activated charge carrier hopping.[31] A summary of these two de-trapping mechanisms is presented in Figure 3f.

Notably, at 80 K and low excitation fluence – where the Auger-assisted mechanism is not active and thermally activated de-trapping is not observed (red traces, Figure 3e) – decay of the trap state bleach intensity is still observed even in the absence of growth of the band edge signal. Within the 3 ns measurement window, ~50% of the trap state population has decayed back to the ground state, indicating that the trap states we observe spectroscopically are possible recombination centers that negatively affect QD device efficiencies.

Quantum Dot Dimers are a Source of Trap States

While the photophysical behavior of the trap state closely resembles that of larger QDs, the presence of anomalously large QDs within the ensemble is not supported by materials characterization. The PbS QDs used in this study are highly monodisperse,[18] with the standard deviation of the mean diameter estimated to be only 3.0% for the 4.2 nm QDs and 1.0% for the 4.9

nm QDs.[31] If the trap states were due to abnormally large QDs in the ensemble, the measured trap state energies would correspond to QDs with diameters of 4.7 nm for 4.2 nm batch and 5.4 nm for the 4.9 nm batch, which is 5-10 standard deviations away from the mean (Figure S6). We do not see evidence for such large QDs in transmission electron microscopy (TEM) images (Figure 4a and previous publications[18, 20]). However, we do occasionally see two QDs that appear to be touching each other. High-resolution (HR-TEM) reveals that some of these QD pairs are epitaxially fused QD dimers (Figure 4b,c), which are expected to have a lower energy than a single QD.[1, 32]

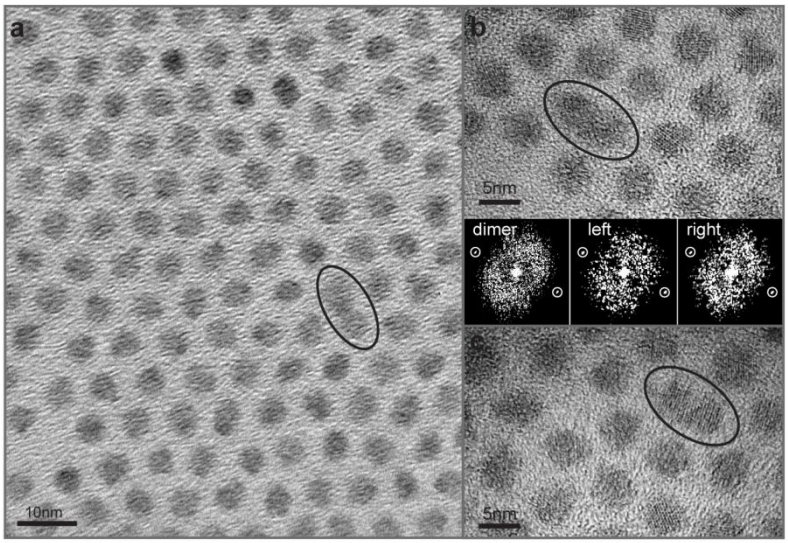

Figure 4. *TEM analysis of epitaxially fused QD dimers.* (a) TEM micrograph of monodisperse 4.9 nm QDs with oleic acid ligands showing an absence of anomalously large QDs, but the presence of a QD dimer. (b) HR-TEM micrograph of an epitaxial dimer. Below the micrograph, selected-area FFT patterns are shown corresponding to either the entire dimer or just the left or right QD. Lattice fringes and FFT analysis show that the QDs are epitaxially connected on the (100) facet. (c) HR-TEM micrograph of an epitaxial dimer with a twinning boundary at the attachment interface.

Intentional formation of PbSe QD dimers during solution phase synthesis has been demonstrated,[32] as has oriented attachment of PbSe QDs to form extended superlattices.[33, 34] Removal of surface ligands using $(NH_4)_2S$ results in connected QD assemblies for PbS, PbSe, CdSe, and CdS QDs, indicating that bare QD surfaces likely attach across a range of materials.[35]

It is therefore reasonable to expect that a few dimers could form unintentionally during standard synthesis and ligand exchange procedures. Selective-area fast Fourier transform (FFT) analysis of the crystal fringes on each half of the QD dimer shown in Figure 4b reveals the relative orientation of the QDs, and their attached crystal facet (see the Supplementary Information and Figure S9 for more detail). We observe fusing predominantly on the {100} facets in our QD dimers. Oriented attachment of PbSe QDs also proceeds along the {100} facets.[33, 34] Increased likelihood of fusing on the {100} facet may be a result of more weakly bound ligands and a greater chance of a bare surface on this facet as compared to the {111} facet.[36]

As shown in Figure 2e & 2l, trap states are already present before ligand exchange and are even observed in solution (Figure S7), indicating that some dimers are formed during the initial synthesis and handling. Previous work showed that intentionally-prepared dimers are not separated from single QDs by size-selective precipitation using common solvent/non-solvent pairs,[32] so they are not likely to be removed during usual purification steps. Based on comparison of the initial bleach intensity in Figure 2a-e, we conclude that additional dimers are also formed during the solid-state ligand exchange step, increasing the trap state density by 50% to 100% following ligand exchange. In samples made with QDs synthesized using lead oxide or lead acetate precursors in octadecene and oleic acid,[37-39] dimer trap states were not observed in QD solids with the native oleic acid ligands, but were observed following ligand exchange (Figure S8).

Hughes *et al.*[32] previously observed energetic splitting between the single QD and QD dimer levels, which decreased with increasing QD size from ~150 meV for 3 nm QDs to ~50 meV for 7 nm QDs.[32] This size-dependent trend in the energy splitting was explained using a tight binding model based on the effective mass approximation and spherical wave functions, with faceted QDs represented by spherical QDs of equivalent volume.[32, 40] This model predicts slightly

shallower trap state depth than the ~100-200 meV we observe in our 4 to 5 nm faceted PbS QDs, but the size-dependent trend is consistent (Figure S6).

To elucidate the origin of the trap states, we performed density function theory (DFT) calculations. Prototype PbS QD (d = 2.0 nm) dimers fused along the {100} facet without surface ligands are considered in this work. A series of dimers were constructed to represent various degrees of fusing, as illustrated in Figure 5a, and their electronic structures and absorption spectra are compared with a single QD (Figure 5b, 5c, 5d). The computed bandgap (~1.0 eV) of our 2 nm QD is underestimated compared to experiment due to the well-known DFT underestimation of semiconductor bandgaps, although trends are typically well represented. In addition, the inclusion of spin-orbit coupling, which is important for describing the electronic structure of lead chalcogenide quantum dots, is known to further reduce the bandgap.[41, 42] The calculated bandgaps of the dimers decrease as the fusing increases, which agrees with previous work in which the energy splitting increases as the overlap between the QDs increases.[32]

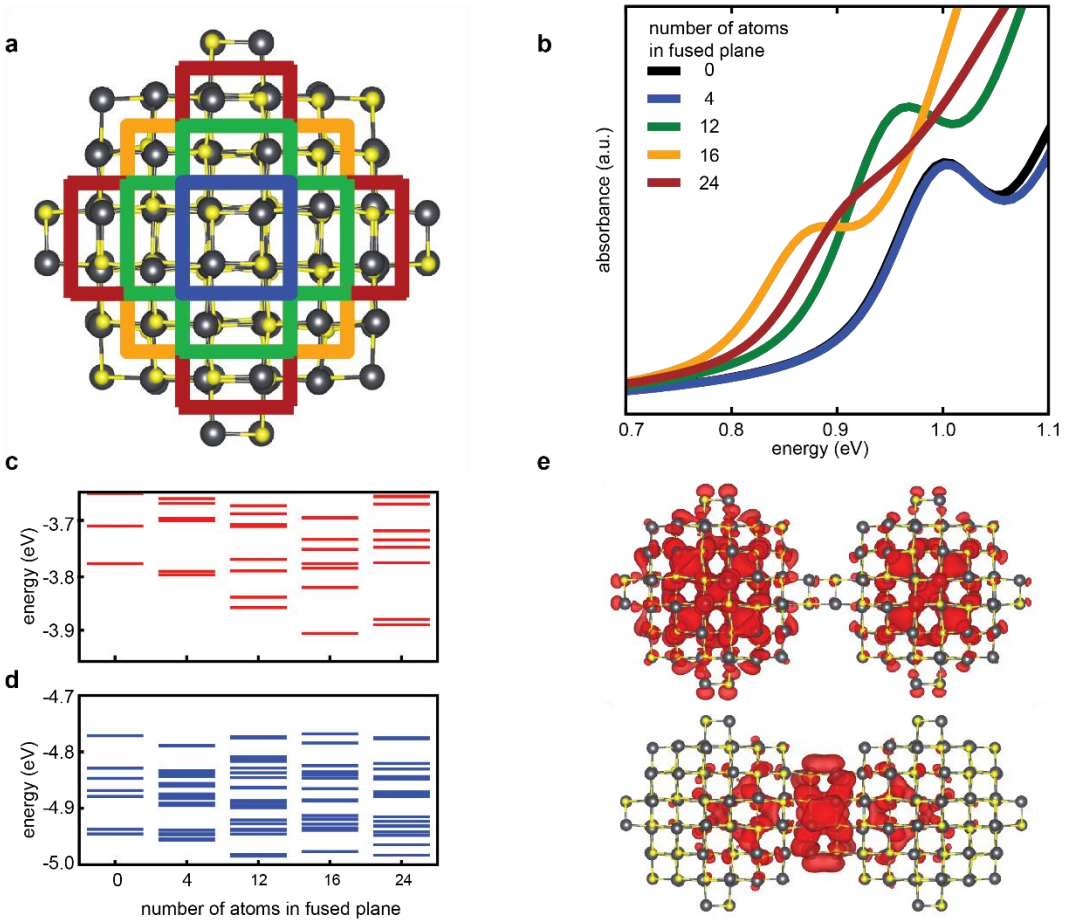

Figure 5. *DFT simulations of PbS QD dimers.* (a) Sideview of the 2 nm diameter single PbS QD. Pb and S atoms are represented by black and yellow spheres respectively. The colored boxes represent increasing degree of fusing in the QD dimers, from 4 (blue) to 12 (green), 16 (orange), and 24 (red) atoms. The fusing occurs along the {100} facet. (b-d) The absorption spectra (b) and unoccupied orbital (c) and occupied orbital (d) energies of fused dimers, compared with a single isolated QD (0 fused atoms). (e) The wavefunction of the LUMO of a dimer with 4 atoms in the fused plane (top), and 12 atoms in the fused plane (bottom).

Figure 5b shows the absorption spectra calculated within the single particle approximation. The first excitonic peaks of the dimers are generally redshifted compared to the single QD, with the absorption coefficient on the same order of magnitude. Surprisingly, when two individual QDs are in direct contact (4 atoms in the fusing plane), there is negligible shift in the first excitonic peak compared to the single QD. This is due to the small hybridization of the wavefunctions when the overlap is small. In fact, the calculated energy splitting between the symmetric and antisymmetric

combinations of the highest occupied molecular orbital (HOMO) and lowest unoccupied molecular orbital (LUMO) of single QDs are less than 10 meV. As the degree of fusing increases to 12, 16, and 24 atoms in the fused plane, there is significant localization of the wavefunction around the fused region, creating new LUMO that are lower in energy than the LUMO of the single QD by around 80-160 meV, as shown in Figure 5c. Given the smaller computed bandgap, the computed LUMO redshifts for the dimers are in general agreement with our experimentally measured values of 150-200 meV. This new state is due to quantum confinement effect in the fused region and cannot be explained using a simple picture of a linear combination of molecular orbitals from individual QDs. These results demonstrate that it is probably the dimer electron level that is shifted relative to neighboring individual dots, as the energies of the highest occupied molecular orbital (HOMO) of the dimers are almost unchanged (Figure 5d). It should be noted that the energy shifts are not directly proportional to the degree of fusing; rather they depend on the exact geometric configuration of the fused region.

We also calculated the electronic structures and absorption spectra for larger QDs (d = 2.5 nm) and their dimers (Figure S10). With a computed bandgap of 0.7 eV for the single QD, the dimer LUMO states are around 25-50 meV lower in energy. As found in the case of smaller QDs, we observe wavefunction localization in the fused region, once a significant degree of fusing (greater than 12 atoms in the fused plane) is introduced.

The energetic shifts attained in these atomistic calculations are consistent with the experimentally measured trap state energies and with the expected size-dependent trend. The number of atoms in the attached facet adds another variable in addition to size dispersity that increases the energetic disorder of QD dimers as compared to single QDs. Thus, we expect a greater linewidth for the ensemble QD dimer absorption as compared to the single QD absorption,

which is observed experimentally for the highly monodisperse QDs. The lowest energy transitions of QD dimers and the degeneracy and absorption cross section of these transitions are consistent with the assignment of trap states in QD solids to QD dimers fused on the {100} facets.

Charge Carrier Equilibrium between Band Edge and Trap State

In Figure 6a, we present photoluminescence spectra of films of ethanethiol-capped 4.9 nm diameter QDs (1.08 eV first absorption peak). At room temperature, we observe emission from the band edge state, but as the temperature decreases, emission from a spectrally distinct lower-energy state grows in. Similar sub-band emission has been observed in lead chalcogenides QDs in a variety of chemical environments.[43-46] Chuang *et al.* identified this state as the likely origin of the large open-circuit voltage deficit in PbS QD photovoltaics.[3] Though the trap state is lower in energy by an amount (~170 meV) many times greater than the available thermal energy at 300 K (~25 meV), the room-temperature emission spectrum is nonetheless dominated by the band edge. This is due to the much greater number of band edge states than trap states, as shown in the schematic in Figure 6b. The PL intensity of each state is proportional to the occupation, *n*, which follows a Boltzmann distribution that accounts for the degeneracies, *g*, of the band edge (BE) and trap states:

$$\frac{PL_{BE}}{PL_{trap}} \propto \frac{n_{BE}}{n_{trap}} = \frac{g_{BE}}{g_{trap}} \exp\left(\frac{-\Delta E}{k_B T}\right), \quad (1)$$

where ΔE is the difference in energy between the trap state and the band edge. If we assume similar radiative efficiency for the band edge and trap states, then the degeneracy ratio and trap state depth can be found by fitting the data to equation (1), as shown in Figure 6c. Note that this fit is valid only at high temperatures (T > 250 K) when charge transfer rates are sufficiently fast to establish equilibrium between the band edge and trap state manifolds.[47, 48] A fit to the data yields a trap state

degeneracy of 1 in ~2500 QDs, which is consistent with other published trap state densities in thiol-treated films measured using a variety of techniques.[11, 16, 49-51] The fitted activation energy of ~180 meV is approximately equal to the energy difference between the band gap and trap state PL features, further reinforcing the assumption of equilibrium which is implicit in the use of Equation 1.

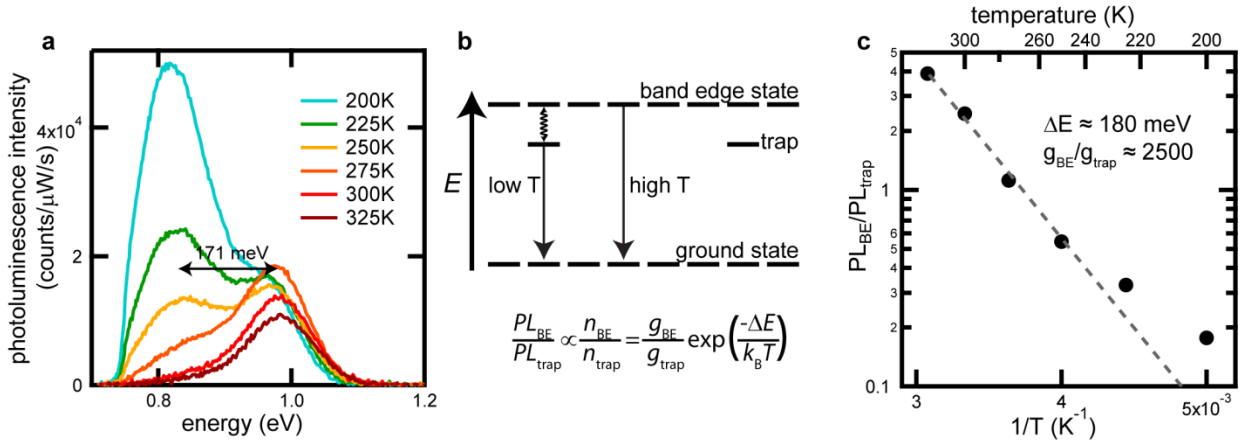

Figure 6. *Emission from band edge and trap states in ethanethiol-treated PbS QD solids.* (a) Photoluminescence spectra as a function of temperature showing PL from the band edge state at room temperature and from the trap state at lower temperatures. (b) Schematic showing much higher density of states at the band edge than at the trap state energy, so that at room temperature, charge carrier occupation of band edge states is entropically favored. (c) Ratio of band edge to trap state PL as a function of temperature (filled circles). A fit (dashed line) gives the trap state depth and density.

To further confirm that thermal equilibrium between band edge states and trap states can be established with a trap state density of 1 in ~ 2500 QDs, we performed Kinetic Monte Carlo (KMC) simulations in model QD solids with different trap state densities at various temperatures. In our model, we follow a free carrier (electron or hole) undergoing a series of stochastic hops between individual QDs. We describe the hopping rate using the Miller-Abrahams rate equations (see Methods section for more details). To highlight the temperature-activated charge carrier de-trapping dynamics, we assume the hopping rate prefactor, as well as other material specific parameters, to be temperature-independent. These simulations include fast recombination through

the trap state (contributing to the simulated trap state population dynamics), but do not include the Auger-assisted de-trapping pathway. Figure 7a explores the effect of trap state density on the occupation probability at T = 300 K. At lower trap state density, more uphill thermalization is observed, which is consistent with the experimentally observed entropically-driven de-trapping mechanism. In Figure 7b, we simulated the effect of temperature on the occupation probability of the band edge and trap states. Growth of the band edge state occupancy is observed within the simulation time window at 300 K but not at lower temperatures, which is consistent with the thermally activated hopping mechanism and associated experimental data shown in Figure 3.

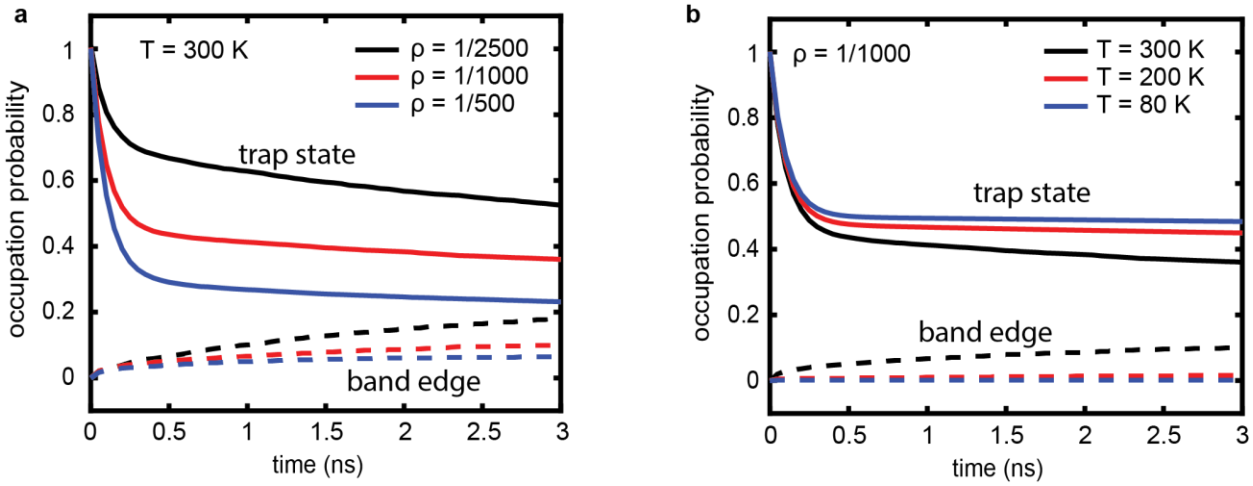

Figure 7. *Kinetic Monte Carlo simulations for de-trapping kinetics at various temperatures and trap densities.* (a) Occupation probability of the band edge state and the trap state as a function of time at various trap state densities. (b) Occupation probability of the band edge state and the trap state as a function of time at different temperatures.

Conclusions and Outlook

In light of the assignment of traps in PbS QD solids to QD dimers we re-examine the literature, which has generally assigned trap states to QD surfaces. Changes in the trap state density as a result of different ligand treatments[9, 50] may reflect a change in the likelihood of QDs fusing, rather than the creation of surface defects. Bozyigit *et al.*[52] used thermal admittance spectroscopy

to measure the spectrum of electronic trap states in PbS QD solids, and found a trap state spectrum that looks similar to a QD absorption spectrum, consistent with our findings from atomistic simulations of QD dimers. Speirs *et al.*[53] observed a reduced trap state density and 147 meV increase in the open-circuit voltage in PbS QD solar cells following overgrowth of a CdS shell. We propose that the CdS shell achieves these results by preventing dimer formation, rather than by passivating surface defects. Furthermore, in light of the de-trapping mechanisms we have observed (Figure 3f), the observation of electrical current in response to optical excitation below the band edge may result from charge carrier de-trapping and transport through band edge states, rather than transport through mid-gap states.[54]

Future efforts must carefully optimize QD synthesis and device fabrication procedures to avoid the accidental formation of dimers, as they can significantly inhibit QD device performance even at very low concentrations of 1 in ~1000 QDs. Improved separation techniques beyond size-selective precipitations are needed to remove dimers that form during synthesis. Since additional dimers also readily form during solid state ligand exchange, solution-phase ligand exchanges,[55, 56] followed by purification to remove any dimers, may be required to form strongly coupled QD solids free of dimer trap states that can ultimately boost QD device efficiency.

Finally, we acknowledge that there may be additional trap states that impact electrical device measurements that cannot be characterized using the optical techniques demonstrated here. Photoluminescence and absorption are sensitive only to states with non-vanishing transition dipole moment. Charge-separated states, such as electron or hole surface traps, may impact QD device efficiency but may not be observable using the techniques employed in this study.

Experimental Methods

PbS QD synthesis and QD solids preparation: The 4.2 nm QDs were synthesized according to Zhang *et al*.[19] and the 4.9 nm QDs were synthesized according to Weidman *et al*.[18] Both syntheses use $PbCl_2$ in oleylamine, but the Zhang synthesis uses bis(trimethylsilyl)sulfide ($(TMS)_2S$), while the Weidman synthesis uses elemental sulfur. The native oleylamine ligands were replaced with oleic acid (oleate) ligands during purification steps following synthesis. Purified QDs were re-dispersed in toluene at a concentration of 100 mg/mL in a nitrogen glovebox. 40 μL of this solution was spin cast at 1500 rpm for 30 s onto a 0.5 inch square borosilicate glass slide (Schott D-263 from Thermo Fisher) that had been cleaned and treated overnight with 0.02M (3-mercaptopropyl)trimthoxysilane (Sigma-Aldrich, 95%) solution in toluene to improve QD adhesion. Some samples were then placed in a 0.1M solution of the desired ligand (1-ethanethiol (Sigma Aldrich, 97%), 1-butanethiol (Sigma Aldrich, 99%), 1-octanethiol (Sigma Aldrich, 98.5%), 1-dodecanethiol (Sigma Aldrich, ≥98%), or 3-mercaptopropionic acid (Sigma Aldrich, ≥99%) in acetonitrile for 24 hours for ligand exchange. The ligand exchange for tetrabutylammonium iodide (Sigma Aldrich, ≥99%) was done at a concentration of 10 mg/mL in methanol, and allowed to sit on the sample for 30 s before spinning to remove and then washing with pure methanol. This created films that were ~100-200 nm thick and have an optical density of ~0.1 at the first absorption peak. Prior to ligand exchange, the QDs are air stable. Following ligand exchange, the samples were kept in an inert environment at all times, including during TA and PL measurements.

Photoluminescence (PL) spectroscopy: Photoluminescence spectra were collected using a 785nm narrow-band continuous wave diode laser. Photoluminescence spectra were collected in a Janis ST-100 cryostat, which was loaded inside the glovebox to prevent air exposure. The laser was focused onto the sample using a 125mm lens at ~30° from the normal, and emitted light was

collected using a backscattered geometry with a 75mm lens and sent to a Bayspec NIR spectrometer. The total power density was 0.2 W/cm^2 at the sample.

Transient absorption (TA) spectroscopy: Transient absorption spectroscopy was performed at the Advanced Optical Spectroscopy and Microscopy Facility at the Center for Functional Nanomaterials at Brookhaven National Laboratory. A commercial Ti:sapphire femtosecond regenerative amplifier (SpectraPhysics Spitfire Pro) operating at a 1 kHz repetition rate was used to generate 800 nm fundamental. An optical parametric amplifier (LightConversion) was used to generate IR pump pulses (1150nm, 1200nm, 1250nm, or 1350nm) with ~100 fs time resolution. A longpass filter (Thorlabs) 50nm shorter than the pump pulse wavelength (e.g. 1200nm longpass for 1250nm pump) was used to clean up the pump line to ensure it did not inadvertently excite higher energy states. The probe pulses were generated by focusing a small portion of the 800 nm fundamental onto a sapphire crystal to generate a white-light supercontinuum over the range of 850–1600 nm. The probe light was split into signal and reference beams, which were detected on a shot-by-shot basis by fiber-coupled InGaAs diode arrays coupled to a high-speed data acquisition system (Ultrafast Systems). The pump-probe time delay was controlled by a mechanical delay stage (Newport). Each measurement is an average of several scans of the delay stage to ensure that dynamics were not changing with laser exposure time. Probe power was typically only a few hundred nanowatts. The pump power to excite the trap state was 300 μW to 2.7 mW, but a significant portion of this light was scattered or transmitted through the sample because the trap state density is low and, as a result, the absorbance at those wavelengths is low.

Transmission electron microscopy (TEM): Transmission electron microscopy (TEM) was performed on a JEOL 2011 instrument operating at 200 kV. High Resolution TEM (HRTEM) images were collected on a JEOL 2010 instrument operating at 200kV. Samples were prepared by

drop casting QD suspensions in hexanes onto copper TEM grids coated with an amorphous carbon support film.

Photothermal deflection spectroscopy (PDS): The PDS was performed according to Jean *et al.*[25] Briefly, the QDs were deposited on custom 4 mm * 12 mm fused quartz slivers. The pump beam consists of a 300 W Xe arc lamp chopped at 10 Hz, a dual-grating monochromator with 1 mm slits, a periscope, and achromatic lenses to collimate and focus the beam. The sample film was secured using a custom holder in a standard 10 mm quartz cuvette. The probe beam consists of a 658 nm, 40 mW temperature-controlled laser diode, an anamorphic prism pair, spatial filter, and iris to circularize the beam and isolate the fundamental mode; a bandpass filter to eliminate scattered light; and a quadrant detector with built-in transimpedance amplifier.

Density functional theory (DFT) calculations: All DFT calculations were performed using the Vienna Ab initio Simulation Package (VASP, v5.4.4).[57, 58] The semi-local Perdew-Burke-Ernzerhof (PBE) generalized gradient approximation[59] is used for the exchange correlation functional. Electronic wavefunctions were expanded in plane waves basis with an energy cutoff of 400 eV. The Pb $5d^{10}6s^26p^2$ and S $3s^23p^6$ electrons were included in the valence, and the core-valence interaction was treated by the projector augmented wave (PAW) method.[60] Spin-orbit coupling effects are included for all atoms.[61] A vacuum spacing of 15 Å was added to the supercell in all three spatial directions to remove any spurious interactions, and only gamma k-point is sampled. The total energies were converged to 10^{-6} eV and the atomic positions were relaxed until the residual forces were less than 0.01eV/ Å. The frequency dependent dielectric function was computed using the independent particle approximation. The absorption coefficient, $\alpha(\omega)$ was obtained using the formula $\alpha(\omega) = \frac{\omega}{cn(\omega)}\varepsilon_2(\omega)$, where c is the speed of light in vacuum, $\varepsilon_2(\omega)$ is the imaginary part of the dielectric function, and $n(\omega)$ is the real part of the complex refractive

index, $n^2(\omega) = \frac{1}{2}(\varepsilon_1 + \sqrt{\varepsilon_2^2 + \varepsilon_1^2})$, with $\varepsilon_1(\omega)$ the real part of the dielectric function. Electronic wavefunctions were visualized using the VESTA program.[62]

Kinetic Monte Carlo (KMC) simulations: Numerical simulations of carrier transport in QD solids were performed using a kinetic Monte Carlo (KMC) algorithm in which a free carrier (electron or hole) undergoes a series of stochastic hops between individual quantum dots. The hopping rate for electrons in the conduction band and holes in the valence band from QD *i* to QD *j* was specified using the Miller−Abrahams rate equation,

$$k_{ji}^{(\alpha)} = \begin{cases} k^{(\alpha)} \exp\left(-\frac{(\varepsilon_j - \varepsilon_i)/2}{k_B T}\right); & \varepsilon_j > \varepsilon_i \\ k^{(\alpha)} \quad ; & \varepsilon_j \leq \varepsilon_i, \end{cases} \tag{2}$$

where $k^{(\alpha)}$ is the hopping rate prefactor of a free charge carrier ($\alpha =$ "–" or "+" for an electron or hole, respectively), ε_i is the energy of the *i*th QD, k_B is the Boltzmann constant, and T is the temperature. Here we assume that the hopping rate prefactor is constant over the temperature range we observe to highlight the phenomenon of temperature-activated charge carrier dynamics from trap to band edge states. Therefore, we assumed that material-specific parameters, such as absorption peak energies ($\bar{\varepsilon}$), energetic disorder (σ_{ih}), and QD superlattice structure, in the KMC model remain constant. The QD solid model consists of a three-dimensional periodically replicated cell in a BCC lattice configuration containing N = 32,000 QDs with a fractional trap state density, ρ = (*number of trap states*)*/N*. Each QD is randomly assigned either a band edge absorption energy or a trap state absorption energy, drawn from a Gaussian distribution with a standard deviation, σ_{inh}, and a peak absorption energy, $\bar{\varepsilon}$. For details on the KMC model procedure and parameterization of QD samples, see the Supporting Information.

Acknowledgements

We thank M. Sfeir for assistance with transient absorption measurements and M. Nasilowski for QDs synthesized with lead oxide and lead acetate. This work was supported by the U.S. Department of Energy, Office of Basic Energy Sciences, under Award Number DE-SC0010538 (R.H.G.) and DE-SC0019345 (W.A.T.). W.S.W. was supported by the U.S. National Science Foundation under Award No. 1452857. E.M.Y.L. was supported by a NSF Graduate Research Fellowship under Grant No. 1122374. Y.L. acknowledges the financial support by National Science Scholarship from Singapore. This research used resources of the Center for Functional Nanomaterials, which is a U.S. DOE Office of Science Facility, at Brookhaven National Laboratory under Contract No. DE-SC0012704. This research used the computational resources of the National Energy Research Scientific Computing Center, a DOE Office of Science User Facility supported by the Office of Science of the U.S. Department of Energy under Contract No. DE-AC02-05CH11231 and Extreme Science and Engineering Discovery Environment (XSEDE), which is supported by National Science Foundation grant number ACI-1053575.

Author contributions

RHG conceived the project, prepared samples, and collected and analyzed transient absorption and photoluminescence data with assistance from WSW under the supervision of WAT. NSD collected and analyzed TEM images. MCW synthesized quantum dots and advised on TEM analysis. YL performed DFT calculations and analyzed computational results with input from HL under the supervision of JCG. EMYL performed kinetic Monte Carlo calculations and analyzed results under the supervision of APW. JJ and WSW collected and analyzed photothermal deflection spectroscopy data under the supervision of VB. RHG, WSW, and WAT wrote the manuscript with contributions from the other authors.

Additional information

Supplementary information is available in the online version of the paper: Additional transient absorption data, photothermal deflection spectroscopy showing sub-bandgap absorption for QD solids, absorption cross section calculation for trap states, trap state depth calculation, FFT analysis of HR-TEM images, additional DFT results, temperature-dependent photoluminescence intensity from 5 K to 300 K, transient photoluminescence data, and KMC model procedure and parameterization. Correspondence should be addressed to W.A.T.

Competing financial interests

The authors declare no competing financial interests.

References

1. Guyot-Sionnest, P. *Journal of Physical Chemistry Letters* **2012,** 3, (9), 1169-1175.
2. Kagan, C. R.; Murray, C. B. *Nat Nanotechnol* **2015,** 10, (12), 1013-26.
3. Chuang, C. H. M.; Maurano, A.; Brandt, R. E.; Hwang, G. W.; Jean, J.; Buonassisi, T.; Bulovic, V.; Bawendi, M. G. *Nano Letters* **2015,** 15, (5), 3286-3294.
4. Zhitomirsky, D.; Voznyy, O.; Levina, L.; Hoogland, S.; Kemp, K. W.; Ip, A. H.; Thon, S. M.; Sargent, E. H. *Nat Commun* **2014,** 5, 3803.
5. Nagpal, P.; Klimov, V. I. *Nat Commun* **2011,** 2, 486.
6. Zhang, Y. J.; Zherebetskyy, D.; Bronstein, N. D.; Barja, S.; Lichtenstein, L.; Schuppisser, D.; Wang, L. W.; Alivisatos, A. P.; Sameron, M. *Nano Letters* **2015,** 15, (5), 3249-3253.
7. Gao, J. B.; Nguyen, S. C.; Bronstein, N. D.; Alivisatos, A. P. *ACS Photonics* **2016,** 3, (7), 1217-1222.
8. Bakulin, A. A.; Neutzner, S.; Bakker, H. J.; Ottaviani, L.; Barakel, D.; Chen, Z. *Acs Nano* **2013,** 7, (10), 8771-8779.
9. Ip, A. H.; Thon, S. M.; Hoogland, S.; Voznyy, O.; Zhitomirsky, D.; Debnath, R.; Levina, L.; Rollny, L. R.; Carey, G. H.; Fischer, A.; Kemp, K. W.; Kramer, I. J.; Ning, Z. J.; Labelle, A. J.; Chou, K. W.; Amassian, A.; Sargent, E. H. *Nature Nanotechnology* **2012,** 7, (9), 577-582.
10. Wanger, D. D.; Correa, R. E.; Dauler, E. A.; Bawendi, M. G. *Nano Lett* **2013,** 13, (12), 5907-12.
11. Bozyigit, D.; Volk, S.; Yarema, O.; Wood, V. *Nano Letters* **2013,** 13, (11), 5284-5288.
12. Hwang, G. W.; Kim, D.; Cordero, J. M.; Wilson, M. W. B.; Chuang, C. M.; Grossman, J. C.; Bawendi, M. G. *Adv Mater* **2015,** 27, (30), 4481-4486.
13. Guyot-Sionnest, P. *J Phys Chem Lett* **2012,** 3, (9), 1169-75.
14. Ip, A. H.; Kiani, A.; Kramer, I. J.; Voznyy, O.; Movahed, H. F.; Levina, L.; Adachi, M. M.; Hoogland, S.; Sargent, E. H. *ACS Nano* **2015,** 9, (9), 8833-8842.
15. Li, H. S.; Zhitomirsky, D.; Dave, S.; Grossman, J. C. *ACS Nano* **2016,** 10, (1), 606-614.
16. Zhitomirsky, D.; Voznyy, O.; Hoogland, S.; Sargent, E. H. *ACS Nano* **2013,** 7, (6), 5282-5290.
17. Hughes, B. K.; Blackburn, J. L.; Kroupa, D.; Shabaev, A.; Erwin, S. C.; Efros, A. L.; Nozik, A. J.; Luther, J. M.; Beard, M. C. *J Am Chem Soc* **2014,** 136, (12), 4670-9.
18. Weidman, M. C.; Beck, M. E.; Hoffman, R. S.; Prins, F.; Tisdale, W. A. *ACS Nano* **2014,** 8, (6), 6363-6371.

19. Zhang, J. B.; Gao, J. B.; Miller, E. M.; Luther, J. M.; Beard, M. C. *ACS Nano* **2014,** 8, (1), 614-622.
20. Weidman, M. C.; Yager, K. G.; Tisdale, W. A. *Chemistry of Materials* **2015,** 27, (2), 474-482.
21. Gilmore, R. H.; Lee, E. M. Y.; Weidman, M. C.; Willard, A. P.; Tisdale, W. A. *Nano Letters* **2017,** 17, (2), 893-901.
22. An, J. M.; Franceschetti, A.; Zunger, A. *Nano Letters* **2007,** 7, (7), 2129-2135.
23. Gao, J.; Johnson, J. C. *ACS nano* **2012,** 6, (4), 3292-3303.
24. Erslev, P. T.; Chen, H. Y.; Gao, J. B.; Beard, M. C.; Frank, A. J.; van de Lagemaat, J.; Johnson, J. C.; Luther, J. M. *Physical Review B* **2012,** 86, (15), 155313.
25. Jean, J.; Mahony, T. S.; Bozyigit, D.; Sponseller, M.; Holovský, J.; Bawendi, M. G.; Bulović, V. *ACS Energy Letters* **2017,** 2, (11), 2616-2624.
26. Klimov, V. I. *Annual Review of Physical Chemistry* **2007,** 58, 635-673.
27. Trinh, M. T.; Sfeir, M. Y.; Choi, J. J.; Owen, J. S.; Zhu, X. *Nano Lett* **2013,** 13, (12), 6091-7.
28. Cademartiri, L.; Montanari, E.; Calestani, G.; Migliori, A.; Guagliardi, A.; Ozin, G. A. *Journal of the American Chemical Society* **2006,** 128, (31), 10337-10346.
29. Zhu, H. M.; Yang, Y.; Hyeon-Deuk, K.; Califano, M.; Song, N. H.; Wang, Y. W.; Zhang, W. Q.; Prezhdo, O. V.; Lian, T. Q. *Nano Letters* **2014,** 14, (3), 1263-1269.
30. Olshansky, J. H.; Ding, T. X.; Lee, Y. V.; Leone, S. R.; Alivisatos, A. P. *Journal of the American Chemical Society* **2015,** 137, (49), 15567-15575.
31. Gilmore, R. H.; Lee, E. M.; Weidman, M. C.; Willard, A. P.; Tisdale, W. A. *Nano Lett* **2017,** 17, (2), 893-901.
32. Hughes, B. K.; Blackburn, J. L.; Kroupa, D.; Shabaev, A.; Erwin, S. C.; Efros, A. L.; Nozik, A. J.; Luther, J. M.; Beard, M. C. *Journal of the American Chemical Society* **2014,** 136, (12), 4670-4679.
33. Geuchies, J. J.; van Overbeek, C.; Evers, W. H.; Goris, B.; de Backer, A.; Gantapara, A. P.; Rabouw, F. T.; Hilhorst, J.; Peters, J. L.; Konovalov, O.; Petukhov, A. V.; Dijkstra, M.; Siebbeles, L. D. A.; van Aert, S.; Bals, S.; Vanmaekelbergh, D. *Nature Materials* **2016,** 15, (12), 1248-1254.
34. Whitham, K.; Yang, J.; Savitzky, B. H.; Kourkoutis, L. F.; Wise, F.; Hanrath, T. *Nature Materials* **2016,** 15, (5), 557-563.
35. Zhang, H. T.; Hu, B.; Sun, L. F.; Hovden, R.; Wise, F. W.; Muller, D. A.; Robinson, R. D. *Nano Letters* **2011,** 11, (12), 5356-5361.
36. Choi, J. J.; Bealing, C. R.; Bian, K. F.; Hughes, K. J.; Zhang, W. Y.; Smilgies, D. M.; Hennig, R. G.; Engstrom, J. R.; Hanrath, T. *Journal of the American Chemical Society* **2011,** 133, (9), 3131-3138.
37. Hines, M. A.; Scholes, G. D. *Advanced Materials* **2003,** 15, (21), 1844-1849.
38. Zhao, N.; Osedach, T. P.; Chang, L. Y.; Geyer, S. M.; Wanger, D.; Binda, M. T.; Arango, A. C.; Bawendi, M. G.; Bulovic, V. *Acs Nano* **2010,** 4, (7), 3743-3752.
39. Chuang, C. H. M.; Brown, P. R.; Bulovic, V.; Bawendi, M. G. *Nature Materials* **2014,** 13, (8), 796-801.

40. Shabaev, A.; Efros, A. L.; Efros, A. L. *Nano Letters* **2013,** 13, (11), 5454-5461.
41. Hummer, K.; Grüneis, A.; Kresse, G. *Physical Review B* **2007,** 75, (19), 195211.
42. Wei, S.-H.; Zunger, A. *Physical Review B* **1997,** 55, (20), 13605-13610.
43. Caram, J. R.; Bertram, S. N.; Utzat, H.; Hess, W. R.; Carr, J. A.; Bischof, T. S.; Beyler, A. P.; Wilson, M. W.; Bawendi, M. G. *Nano Lett* **2016,** 16, (10), 6070-6077.
44. Yue, F.; Tomm, J. W.; Kruschke, D. *Physical Review B* **2014,** 89, (8).
45. Harbold, J. M.; Wise, F. W. *Physical Review B* **2007,** 76, (12), 125304.
46. Grodzinska, D.; Evers, W. H.; Dorland, R.; van Rijssel, J.; van Huis, M. A.; Meijerink, A.; Donega, C. D.; Vanmaekelbergh, D. *Small* **2011,** 7, (24), 3493-3501.
47. Zhang, J.; Toentino, J.; Smith, E. R.; Zhang, J. B.; Beard, M. C.; Nozik, A. J.; Law, M.; Johnson, J. C. *Journal of Physical Chemistry C* **2014,** 118, (29), 16228-16235.
48. Gao, J.; Zhang, J.; van de Lagemaat, J.; Johnson, J. C.; Beard, M. C. *ACS nano* **2014,** 8, (12), 12814-12825.
49. Zhitomirsky, D.; Voznyy, O.; Levina, L.; Hoogland, S.; Kemp, K. W.; Ip, A. H.; Thon, S. M.; Sargent, E. H. *Nature Communications* **2014,** 5, 3803.
50. Wanger, D. D.; Correa, R. E.; Dauler, E. A.; Bawendi, M. G. *Nano Letters* **2013,** 13, (12), 5907-5912.
51. Bozyigit, D.; Lin, W. M. M.; Yazdani, N.; Yarema, O.; Wood, V. *Nature Communications* **2015,** 6, 6180.
52. Bozyigit, D.; Yazdani, N.; Yarema, M.; Yarema, O.; Lin, W. M.; Volk, S.; Vuttivorakulchai, K.; Luisier, M.; Juranyi, F.; Wood, V. *Nature* **2016,** 531, (7596), 618-22.
53. Speirs, M. J.; Balazs, D. M.; Fang, H. H.; Lai, L. H.; Protesescu, L.; Kovalenko, M. V.; Loi, M. A. *Journal of Materials Chemistry A* **2015,** 3, (4), 1450-1457.
54. Nagpal, P.; Klimov, V. I. *Nature Communications* **2011,** 2, 486.
55. Lin, Q.; Yun, H. J.; Liu, W.; Song, H. J.; Makarov, N. S.; Isaienko, O.; Nakotte, T.; Chen, G.; Luo, H.; Klimov, V. I.; Pietryga, J. M. *J Am Chem Soc* **2017,** 139, (19), 6644-6653.
56. Liu, M.; Voznyy, O.; Sabatini, R.; Garcia de Arquer, F. P.; Munir, R.; Balawi, A. H.; Lan, X.; Fan, F.; Walters, G.; Kirmani, A. R.; Hoogland, S.; Laquai, F.; Amassian, A.; Sargent, E. H. *Nat Mater* **2017,** 16, (2), 258-263.
57. Kresse, G.; Furthmüller, J. *Physical Review B* **1996,** 54, (16), 11169-11186.
58. Kresse, G.; Furthmüller, J. *Computational Materials Science* **1996,** 6, (1), 15-50.
59. Perdew, J. P.; Burke, K.; Ernzerhof, M. *Physical Review Letters* **1996,** 77, (18), 3865-3868.
60. Kresse, G.; Joubert, D. *Physical Review B* **1999,** 59, (3), 1758-1775.
61. Steiner, S.; Khmelevskyi, S.; Marsmann, M.; Kresse, G. *Physical Review B* **2016,** 93, (22), 224425.
62. Momma, K.; Izumi, F., *VESTA: A Three-Dimensional Visualization System for Electronic and Structural Analysis*. 2008; Vol. 41, p 653-658.

Supplementary Information for

Epitaxial Dimers and Auger-Assisted De-Trapping in PbS Quantum Dot Solids

Rachel H. Gilmore[1], Yun Liu[2], Wenbi Shcherbakov-Wu[4], Nabeel S. Dahod[1], Elizabeth M.Y. Lee[1], Mark C. Weidman[1], Huashan Li[2], Joel Jean[3], Vladimir Bulović[3], Adam P. Willard[4], Jeffrey C. Grossman[2], William A. Tisdale[1]*

[1]Department of Chemical Engineering, Massachusetts Institute of Technology, Cambridge, Massachusetts, 02139, USA.

[2]Department of Materials Science and Engineering, Massachusetts Institute of Technology, Cambridge, Massachusetts 02139, USA.

[3]Department of Electrical Engineering and Computer Science, Massachusetts Institute of Technology, Cambridge, Massachusetts, 02139, USA.

[4]Department of Chemistry, Massachusetts Institute of Technology, Cambridge, Massachusetts 02139, USA.

*Correspondence to: tisdale@mit.edu

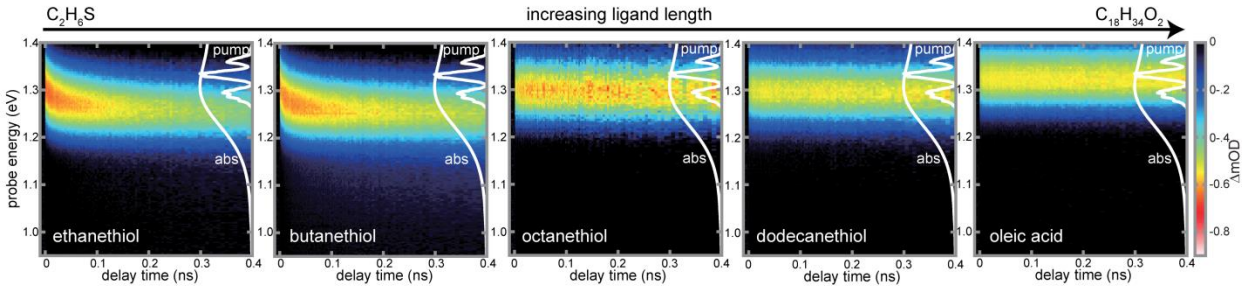

Figure S1. Transient absorption exciting at the band edge peak for QD solids with thiol ligands of varying lengths. A transient redshift indicating charge transport in the observed time window is present for ethanethiol and butanethiol QD solids, but not for octanethiol, dodecanethiol, or oleic acid.

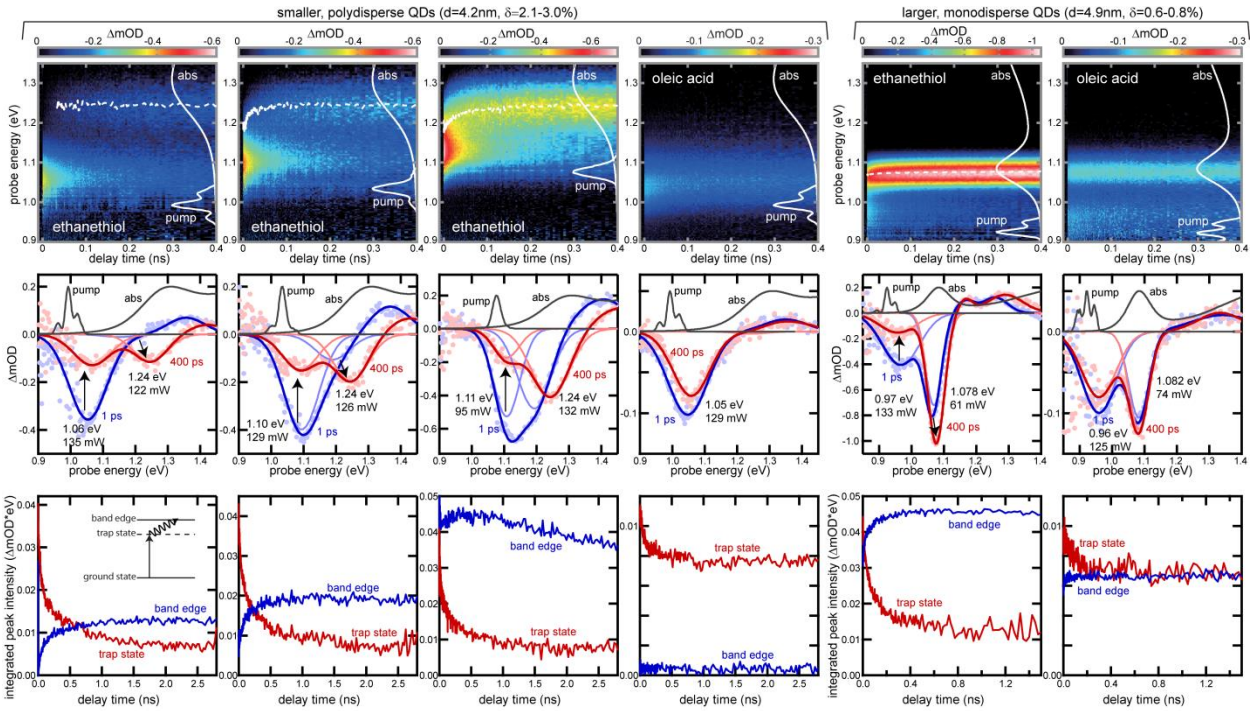

Figure S2. Transient absorption spectroscopy showing excitation of the trap state and upconversion to the band edge state in QD solids with ethanethiol ligands. (top row) Color plots repeated from Figure 2. (middle row) Spectra at 1 ps and 400 ps for the QD solids in the row above. (bottom row) Population dynamics of the band edge and trap states for the QD solids shown in the top row.

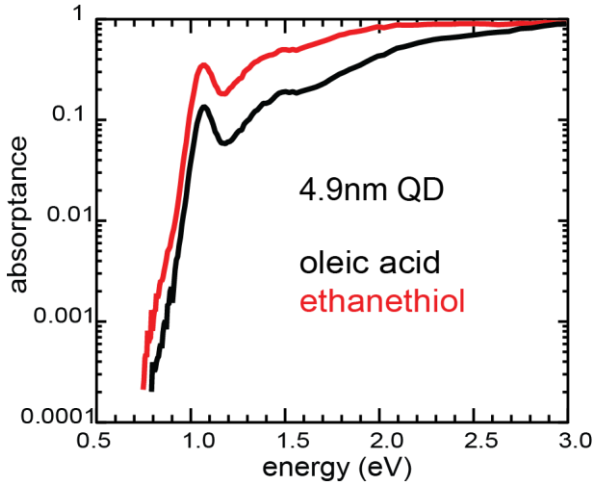

Figure S3. Photothermal deflection spectroscopy showing sub-bandgap absorption of 4.9nm QDs used for the transient absorption measurement. The continuous absorption below the band gap is consistent with the existence of a continuous manifold of trap states.

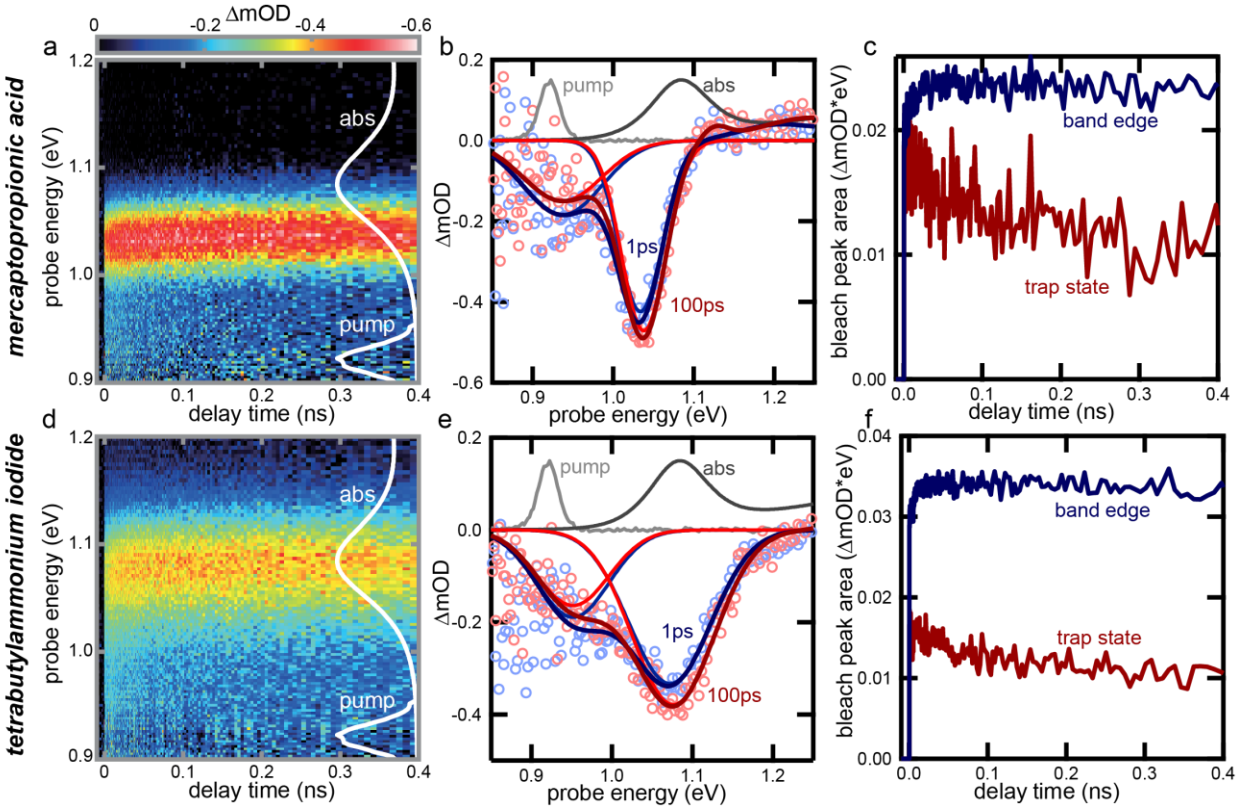

Figure S4. PbS QDs with mercaptopropionic acid (top row) and tetrabutylammonium iodide (bottom row) ligands also show trap state excitation and upconversion to the band edge state.

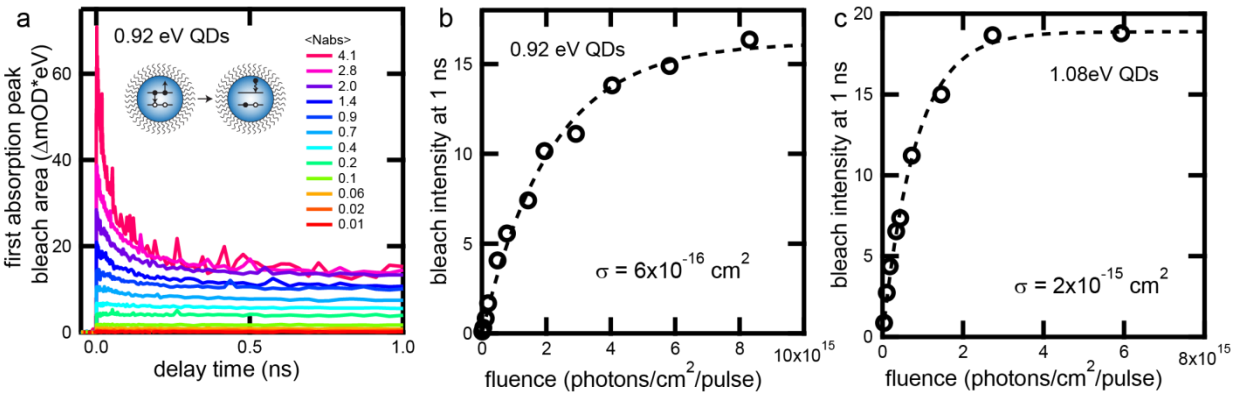

Figure S5. Transient absorption signatures of Auger recombination and calculation of the absorption cross section. (a) Increasing the pump fluence increases the number of absorbed photons per QD. Excitons on QDs with more than 1 exciton undergo Auger recombination, reducing the TA bleach signal in a few hundred picoseconds. (b-c) The absorption cross section can be estimated from a plot of the bleach intensity at 1ns, after Auger recombination is complete

but before appreciable single exciton recombination, versus the excitation fluence. This is shown for 5.8 nm QDs in (b) and 5.0 nm QDs in (c).

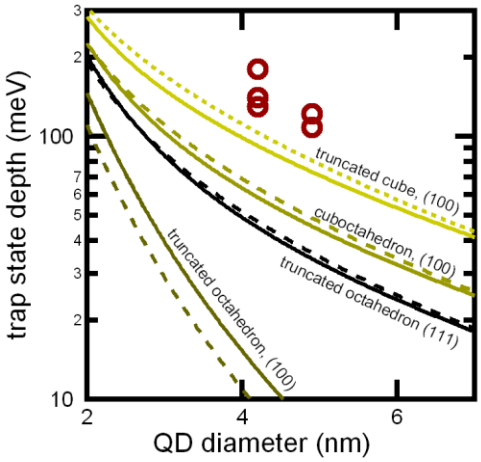

Figure S6. Calculated trap state depth for different QD shapes (truncated octahedron, cuboctahedron, truncated cube) and attached facets ((100), (111)) based on effective mass and tight binding approximations.[1, 2] Calculations with a confining potential barrier of 1.0 eV[1] are shown with solid lines and of 1.6 eV[3] with dashed lines. Trap state depth extracted from transient absorption measurements are shown in red circles.

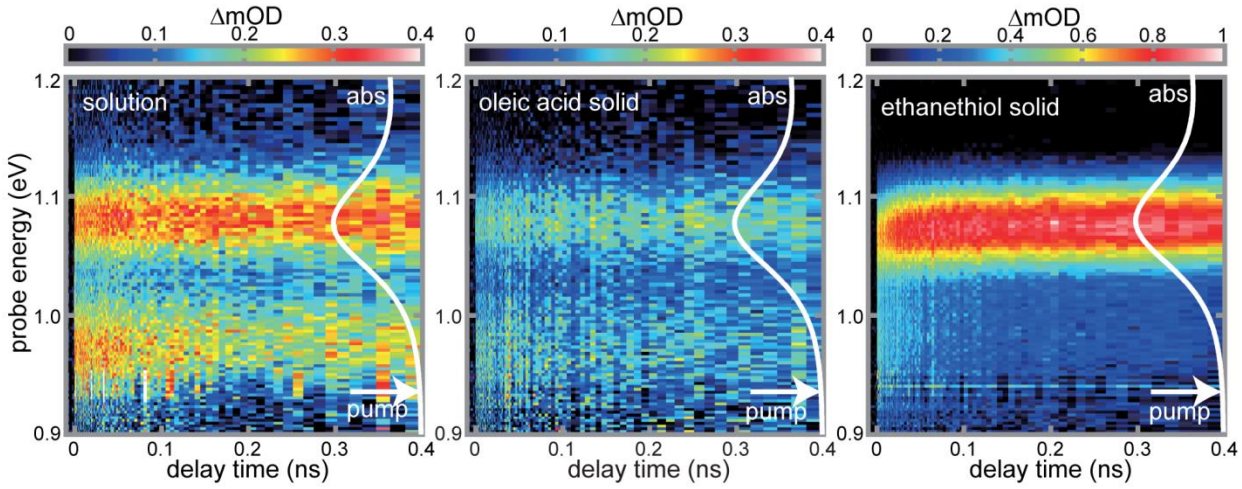

Figure S7. Trap state excitation of oleic acid-capped QDs in solution (left), oleic acid-capped QD solids (center), and following ligand exchange for ethanethiol (right). The optical density at the band edge peak absorption was 0.2 for the solution sample, 0.1 for the oleic acid sample, and 0.08 for the EMT sample. The concentration of trap states is similar in solution and in the oleate-capped QD solid, but is higher in ethanethiol-treated solids, even after accounting for a possible increase in absorption cross section per QD for the shorter ligands[4].

PbS QDs synthesized *via* other methods. QDs made using lead oleate or lead acetate precursors, rather than lead chloride, show no measurable dimer trap state absorption with native oleate ligands, but do show trap state absorption after ethanethiol ligand exchange (Figure S8). There are several possible reasons why the lead chloride and oleylamine synthesis method might result in measurable dimer states, whereas the lead oleate or lead acetate synthesis methods do not. Oleylamine binds weakly to the QD surface and is in rapid equilibrium with free ligand in solution,[5] so it may be easier for ligands to detach and create bare surfaces that may fuse. The dimers might also form during the oleylamine to oleic acid solution ligand exchange step, which is added to purify the QDs and remove unreacted lead chloride. The lead chloride and oleylamine synthesis is capable of producing nearly monodisperse QDs, and more monodisperse QDs may orient and fuse more readily.[6] Additionally, different purification and processing steps might result in different ligand coverage,[7] which could also impact the likelihood of dimer formation. Alternatively, traps may be present at similar rates, but are harder to resolve because of greater inhomogeneous broadening. More work is needed to further understand the role of the synthetic method in dimer formation in order to make monodisperse, homogeneously-broadened, trap-free PbS QD solids.

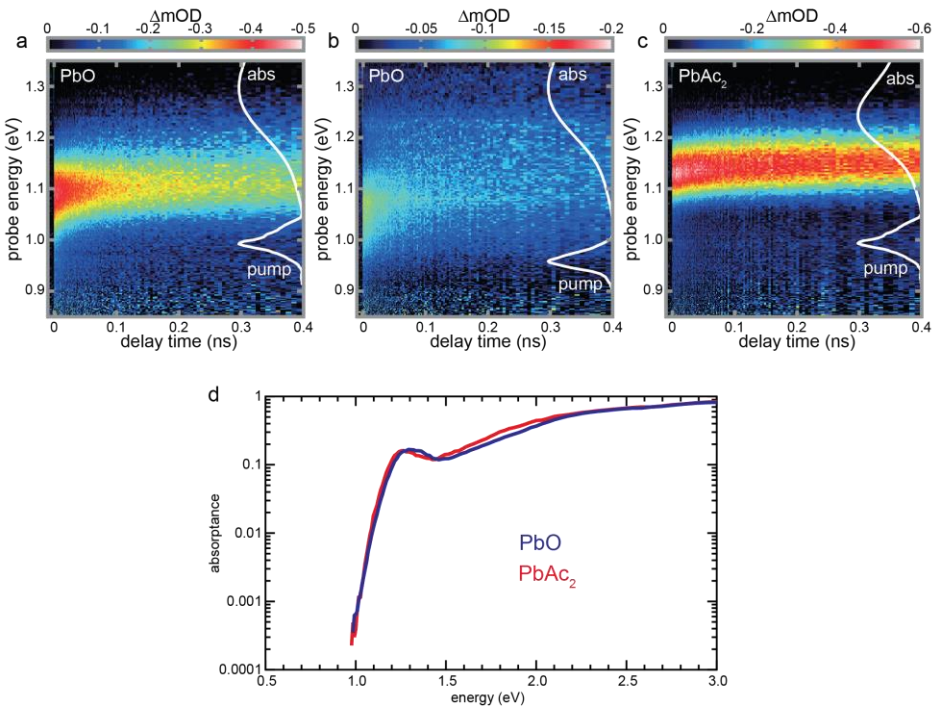

Figure S8. Trap state excitation in ethanethiol-capped QD solids synthesized with PbO (a-b) or $PbAc_2$ (c). Photothermal deflection measurements showing the sub-bandgap absorption are shown in (d).

HR-TEM analysis of PbS QD dimers. To confirm the presence of PbS quantum dot dimers, high resolution TEM images of PbS quantum dot monolayers were collected and analyzed). For this analysis, a dimer is defined as two PbS quantum dots fused together such that they support a single continuous crystal structure throughout both substructures. This is observed *via* clear lattice planes that span the entire dimer with no change in orientation (Figure 4b). In contrast, two unattached quantum dots that are simply in close proximity to one another would not display any alignment between their two lattices. Thus, in order to confirm attachment between two quantum dots that appear to be in contact, analysis of the HR-TEM images must reveal that the constituent nanocrystals are in fact aligned on one of their faces.

This analysis is implemented through inspection of the fast Fourier transform (FFT) of the candidate dimer image. The FFT reveals the orientation and spacing of the lattice planes visualized in HRTEM. For instance, FFT analysis of a HRTEM image of a quantum dot with its 200 plane parallel to the beam would reveal a peak at a 0.31 nm/cycle radial position with respect to the center spot of the FFT. This spacing is confirmed by inspecting the 200 peak in the XRD pattern for PbS. Additionally, the azimuthal position of the spot corresponding to these lattice planes is determined by the angle of the planes with respect to the image. For instance, two QDs in the same image with 200 planes oriented perpendicular to one another would show a difference in azimuthal position of 90 degrees with respect to the corresponding FFT spots. Several QDs in an image oriented randomly will show FFT spots at many azimuthal positions and radial distances (Figure S9).

In analyzing potential dimers, FFTs of both constituents and the entire dimer were used to determine if all showed lattice planes that were aligned with respect to one another. Through this method, we observed PbS quantum dot dimers that were attached across their respective 100 faces (Figure 4b). We also observed one case in which two dots dimerized with a twinning boundary between the constituents (Figure 4c and Figure S9b).

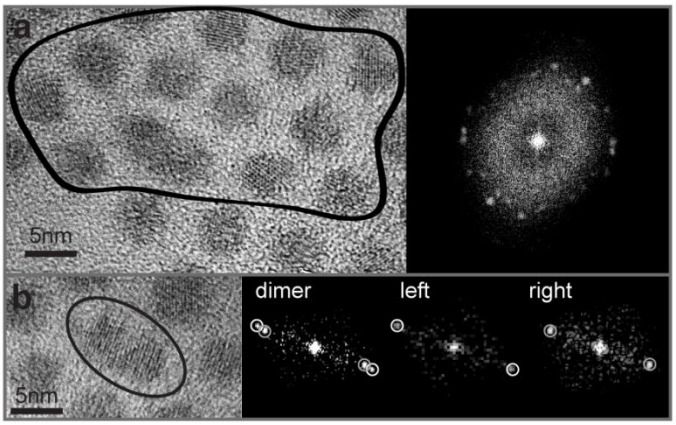

Figure S9. FFT analysis of HR-TEM images. (a) FFT analysis of a monolayer of unattached, randomly oriented QDs shows many FFT spots at different azimuthal positions. (b) FFT analysis for the dimer shown in Figure 4 in the main text.

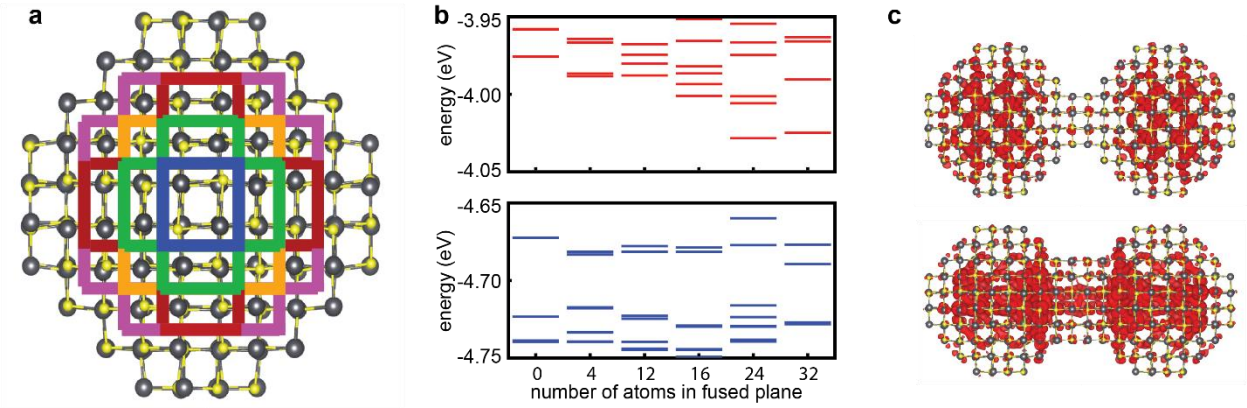

Figure S10. DFT calculations of a 2.5 nm diameter QD. (a) Sideview of the 2.5 nm diameter PbS QD. The black and yellow atoms represent Pb and S respectively. The colored boxes represent increasing degree of fusing in the QD dimers, from 4 to 12, 16, 24, and 32 atoms. The fusing occurs along the (100) facet. (b) Unoccupied orbitals and (c) occupied orbitals of fused dimers compared with single isolated QD. (d) The wavefunction of the LUMO state of a dimer with 12 atoms in the fused plane (top), and that of the fused dimer with 32 atoms in the fused plane (bottom).

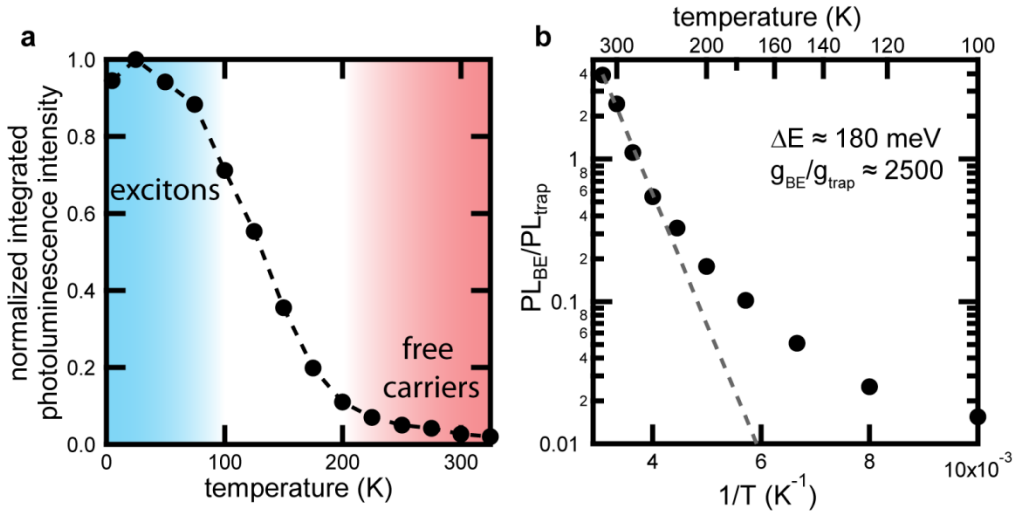

Figure S11. (a) Normalized photoluminescence intensity as a function of temperature. PL efficiency is low near room temperature when excitons rapidly dissociate, and high at low temperatures when charge carriers remain bound as excitons.[8] (b) Arrhenius plot from Figure 6c extended to lower temperatures, illustrating the effects of undissociated excitons and slower exciton transport at lower temperature, which pulls the ratio of band edge to trap state emission further away from the equilibrium line.

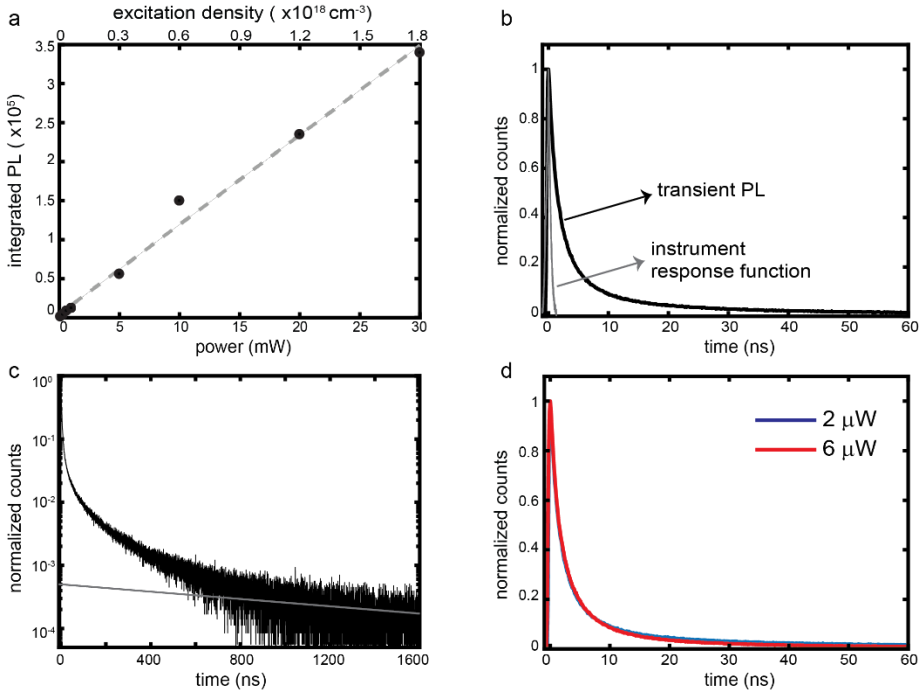

Figure S12. (a) Power dependence of steady-state photoluminescence at 300 K. PL intensity is linearly dependent on power. (b) Transient PL shows a fast decay component, likely due to exciton dissociation, and a slow component corresponding to undissociated exciton radiative decay. The time-averaged power used in this experiment was 2 μW and pulse fluence was 11 nJ/cm^2 at a laser

repetition rate of 125 kHz. (c) Transient PL response under a longer time window. The grey line is the PL lifetime of oleate capped PbS QDs, shown for reference. (d) Transient PL collected at higher laser power (6 μW) showing the same dynamics, indicating that this is the power independent regime.

Kinetic Monte Carlo (KMC) simulations. The inhomogeneous linewidth σ_{inh} for either trap or band edge state has been estimated by fitting a Gaussian to their respective transient absorption bleach intensity. Based on our previous band-edge charge carrier transport studies using a similar technique,[9, 10] we assume that the total linewidth has both homogenous and inhomogeneous contributions in which all the lineshapes are assumed be Gaussians,

$$\sigma_{total}^2(T) = \sigma_{ih}^2 + \sigma_h^2(T) \quad (3)$$

where the temperature-dependent homogenous linewidth $\sigma_h(T)$ is equal for both band edge and trap states absorption features. Table 1 summarizes the list of parameters used in our simulations and their corresponding sources.

Statistics were averaged over 1000 realizations of the QD solid (energetic disorder) at a given trap state density and temperature. Each realization of the QD solid consisted of $6.4X10^7\rho$ single carrier trajectories. Every KMC trajectory started by initializing a free carrier on one of the randomly selected QDs with trap states. 50 % of the QDs with trap states undergo decay with a rate of 10 ns^{-1}.

Table 1. Kinetic Monte Carlo model parameters

State	$\bar{\varepsilon}$ (eV)	σ_{ih} (meV) [a]	$k^{(\alpha)}$ (ns^{-1}) [b]
Trap	1.275	41	17.5
Band edge	1.030	49	17.5

[a] Estimated based on transient absorption measurement study of a similarly sized PbS QDs (4.1 nm in diameter) with homogenous linewidth of 48 meV at T = 300 K. [10]

[b] Estimated based on transient absorption measurement study of a similarly sized PbS QDs (4.1 nm in diameter) at T = 300 K. [10]

References

1. Hughes, B. K.; Blackburn, J. L.; Kroupa, D.; Shabaev, A.; Erwin, S. C.; Efros, A. L.; Nozik, A. J.; Luther, J. M.; Beard, M. C. *J Am Chem Soc* **2014,** 136, (12), 4670-9.
2. Shabaev, A.; Efros, A. L.; Efros, A. L. *Nano Lett* **2013,** 13, (11), 5454-61.
3. Bozyigit, D.; Lin, W. M.; Yazdani, N.; Yarema, O.; Wood, V. *Nat Commun* **2015,** 6, 6180.

4. Geiregat, P.; Justo, Y.; Abe, S.; Flamee, S.; Hens, Z. *Acs Nano* **2013,** 7, (2), 987-993.
5. Moreels, I.; Justo, Y.; De Geyter, B.; Haustraete, K.; Martins, J. C.; Hens, Z. *ACS Nano* **2011,** 5, (3), 2004-2012.
6. Guyot-Sionnest, P. *J Phys Chem Lett* **2012,** 3, (9), 1169-75.
7. Choi, J. J.; Bealing, C. R.; Bian, K.; Hughes, K. J.; Zhang, W.; Smilgies, D. M.; Hennig, R. G.; Engstrom, J. R.; Hanrath, T. *J Am Chem Soc* **2011,** 133, (9), 3131-8.
8. Zhang, J.; Tolentino, J.; Smith, E. R.; Zhang, J.; Beard, M. C.; Nozik, A. J.; Law, M.; Johnson, J. C. *The Journal of Physical Chemistry C* **2014,** 118, (29), 16228-16235.
9. Gilmore, R. H.; Lee, E. M.; Weidman, M. C.; Willard, A. P.; Tisdale, W. A. *Nano Lett* **2017,** 17, (2), 893-901.
10. Gilmore, R. H.; Winslow, S. W.; Lee, E. M. Y.; Ashner, M. N.; Yager, K. G.; Willard, A. P.; Tisdale, W. A. *ACS Nano* **2018,** 12, (8), 7741-7749.